Mercury's Seasonal Sodium Exosphere: MESSENGER Orbital Observations

Timothy A. Cassidy[a], Aimee W. Merkel[a], Matthew H. Burger[b], Rosemary M. Killen[c], William E. McClintock[a], Ronald J. Vervack, Jr.[d], Menelaos Sarantos[e,f]

[a] Laboratory for Atmospheric and Space Physics, University of Colorado, Boulder, CO 80303, USA.

[b] Goddard Earth Sciences, Technology, and Research, Morgan State University, Baltimore, MD 21251, USA.

[c] Solar System Exploration Division, NASA Goddard Space Flight Center, Greenbelt, MD 20771, USA.

[d] The Johns Hopkins University Applied Physics Laboratory, Laurel, MD 20723, USA.

[e] Goddard Planetary Heliophysics Institute, University of Maryland Baltimore County, Baltimore, MD 21250, USA.

[f] Heliophysics Science Division, NASA Goddard Space Flight Center, Greenbelt, MD 20771, USA.

Corresponding author:

Timothy A. Cassidy,
3665 Discovery Drive
Boulder, CO 80303

434-806-9880
timothy.cassidy@lasp.colorado.edu

Abstract

The Mercury Atmospheric and Surface Composition Spectrometer (MASCS) Ultraviolet and Visible Spectrometer (UVVS) on the MErcury Surface, Space ENvironment, GEochemistry, and Ranging (MESSENGER) spacecraft now orbiting Mercury provides the first close-up look at the planet's sodium exosphere. UVVS has observed the exosphere from orbit almost daily for over 10 Mercury years. In this paper we describe and analyze a subset of these data: altitude profiles taken above the low-latitude dayside and south pole. The observations show spatial and temporal variations, but there are no obvious year-to-year variations in most of the observations. We do not see the episodic variability reported by some ground-based observers. We used these altitude profiles to make estimates of sodium density and temperature. The bulk of the exosphere, at about 1200 K, is much warmer than Mercury's surface. This value is consistent with some ground-based measurements and suggests that photon-stimulated desorption is the primary ejection process. We also observe a tenuous energetic component but do not see evidence of the predicted thermalized (or partially thermalized) sodium near Mercury's surface temperature. Overall we do not see the variable mixture of temperatures predicted by most Monte Carlo models of the exosphere.

Keywords: Mercury, Atmosphere; Atmospheres, Structure; Atmospheres, Dynamics; Spectroscopy

Highlights

* We describe the first orbital observations of Mercury's sodium exosphere.
* The sodium exosphere varies spatially and temporally, but most of this variation is seasonally repeatable for the portions of the exosphere that we describe.
* The low-latitude dayside exosphere has a two-temperature structure. The bulk of the exosphere is at about 1200 K throughout the Mercury year.
* There is no evidence of a thermalized or partially thermalized component near Mercury's surface temperature.
* Radiation acceleration (i.e., photon pressure) compresses the exosphere on the dayside.

1. Introduction

The Mercury Atmospheric and Surface Composition Spectrometer (MASCS) Ultraviolet and Visible Spectrometer (UVVS) on the MErcury Surface, Space ENvironment, GEochemistry, and Ranging (MESSENGER) spacecraft has provided almost daily observations of the exosphere since entering orbit about Mercury on 18 March 2011. UVVS uses a variety of observation geometries during each orbital pass, but this paper focuses on altitude profiles, or "limb scans," of sodium emission taken above Mercury's sunlit hemisphere (McClintock and Lankton, 2007). UVVS measures the D_1 and D_2 emission lines near 589 nm wavelength, which are caused by resonant scattering of sunlight. The scattering is so efficient that even the emission visible from Mercury's nightside (on the order of hundreds of kilorayleighs; Baumgardner et al., 2008) is comparable to Earth's brightest visible aurorae (e.g., Hunten et al., 1956).

This paper describes the first orbital observations of Mercury's sodium exosphere. Since its discovery almost three decades ago (Potter and Morgan, 1985), the sodium exosphere has been observed regularly from the ground (see reviews by Domingue et al., 2007, and Killen et al., 2007). The orbital observations described here are quite different from ground-based observations, which can image Mercury's entire disk and surrounding space. The UVVS observations described here, by contrast, are altitude profiles tangent to the surface (Fig. 2) with limited spatial coverage (Fig. 3). UVVS, however,

provides unprecedented spatial resolution and observation cadence. This paper presents 10 Mercury years of near-daily observations that allow us to resolve variations in both local time and true anomaly.

Ground-based observers and modelers have proposed a number of hypotheses to explain their observations. One of the early ideas was that sputter ejection of sodium from Mercury's poles is responsible for variable polar bright spots (Potter and Morgan, 1990; Sarantos et al., 2001). Another is that thermal desorption of sodium at dawn is responsible for the dawn/dusk asymmetry reported by some observers (e.g., Sprague et al., 1997). These observations led to many modeling efforts. The early models began with a few simple assumptions and explored the dynamics of sodium atoms pushed anti-sunward by radiation pressure (Ip, 1986; Smyth and Marconi, 1995). These were superseded by simulations with an increasing number of interdependent source processes (Leblanc and Johnson, 2003; Mura et al., 2009; Leblanc and Johnson, 2010; Burger et al., 2010).

A principal focus of exosphere literature has been temporal variability. Observers have reported *episodic* and *seasonal* (yearly repeatable) variability in the exosphere. Episodic variability is attributed to processes such as short-term changes in solar wind conditions (e.g., Killen et al., 2001; Leblanc et al., 2009; Benna et al., 2010). Seasonal variability is driven by Mercury's changing distance from the Sun, during which the intensities of source, loss, and transport processes change (Lammer et al., 2003; Sarantos et al., 2007, Kameda et al., 2009). In this paper we describe the MESSENGER UVVS results in the context of

this previous work, especially with regard to temporal variability. However, a direct comparison with ground-based observations is difficult, and sometimes impossible, because of the differing nature of the two data sets.

This paper is organized as follows. In Section 2, we describe the UVVS observations and discuss conclusions that can be reached by simple inspection of the data, followed by quantitative analysis of UVVS limb scans to estimate exospheric temperature (Section 3) and density (Section 4). We close with a discussion of implications for exospheric source, loss, and transport processes (Section 5).

2. UVVS observations

2.1. Description of UVVS observations

The UVVS is comprised of a telescope feeding a grating monochromator that scans discrete narrow wavelength bands to detect exosphere emission (McClintock and Lankton, 2007). The sodium spectral scan covers a wavelength range of 587.7 nm to 591.1 nm with a 0.2 nm step size, allowing both the D_1 (589.8 nm) and D_2 (589.1 nm) emission line centers to fall in the middle of the scan. The detected signal is a combination of sodium emission, solar light scattered off of Mercury's surface, and a dark offset (Fig. 1). The dark offset is from thermionic emission within the detector and is a function of instrument temperature. The dark offset is fully characterized and routinely sampled on the

night side of the planet. The scattered sunlight contribution is reflected off of Mercury's surface and scattered into the monochromator. This component is determined by fitting a solar continuum spectrum to the dark-subtracted spectral scan using only wavelengths near the ends of the scan away from the emission lines. The dark and scattered light components are subtracted from the measured signal, and the residual is assumed to be sodium emission from the exosphere. The instrument radiometric sensitivity calibration is applied to convert from counts per second to radiance, and the 11 points around the two line (D_1 and D_2) centers are summed to obtain a total sodium radiance value in kilorayleighs (kR) for each spectral scan. Each limb scan presented in this paper is made up of a series of spectral measurements as the instrument scans in altitude (Fig. 2 and Fig. 4). As mentioned earlier, sodium emission is as bright as the Earth's visible aurorae, making it very easy to detect. Therefore the sodium emission dominates the detected signal and the dark and solar scattering components are only small sources of retrieval error as shown in Fig. 1.

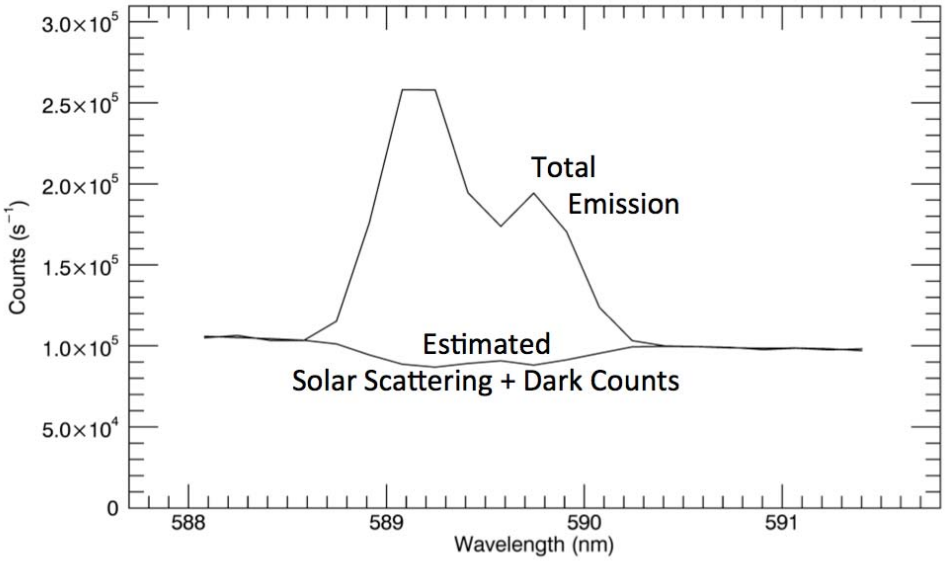

Fig. 1. Example spectrum of sodium D_1 and D_2 emission observed by MESSENGER UVVS at ~100 km tangent altitude near the subsolar point. The graph shows the total observed counts s^{-1} along with the estimated solar scattering and dark offset backgrounds. The observation was taken on 23 May 2012.

In this paper we describe two MESSENGER UVVS observation types, dayside limb scans and south pole limb scans, obtained between 5 April 2011 and 29 July 2013. Dayside limb scans provide most of the data analyzed in this paper. An example of the observation geometry is shown at the top of Fig. 2. The dayside limb scans are taken when the MESSENGER spacecraft is near apogee and the UVVS line-of-sight points approximately northward. UVVS dayside limb scans provide altitude profiles at primarily low latitudes from dawn to dusk. Each altitude profile extends from just above the surface, as low as 10 km, to several thousand kilometers above the surface.

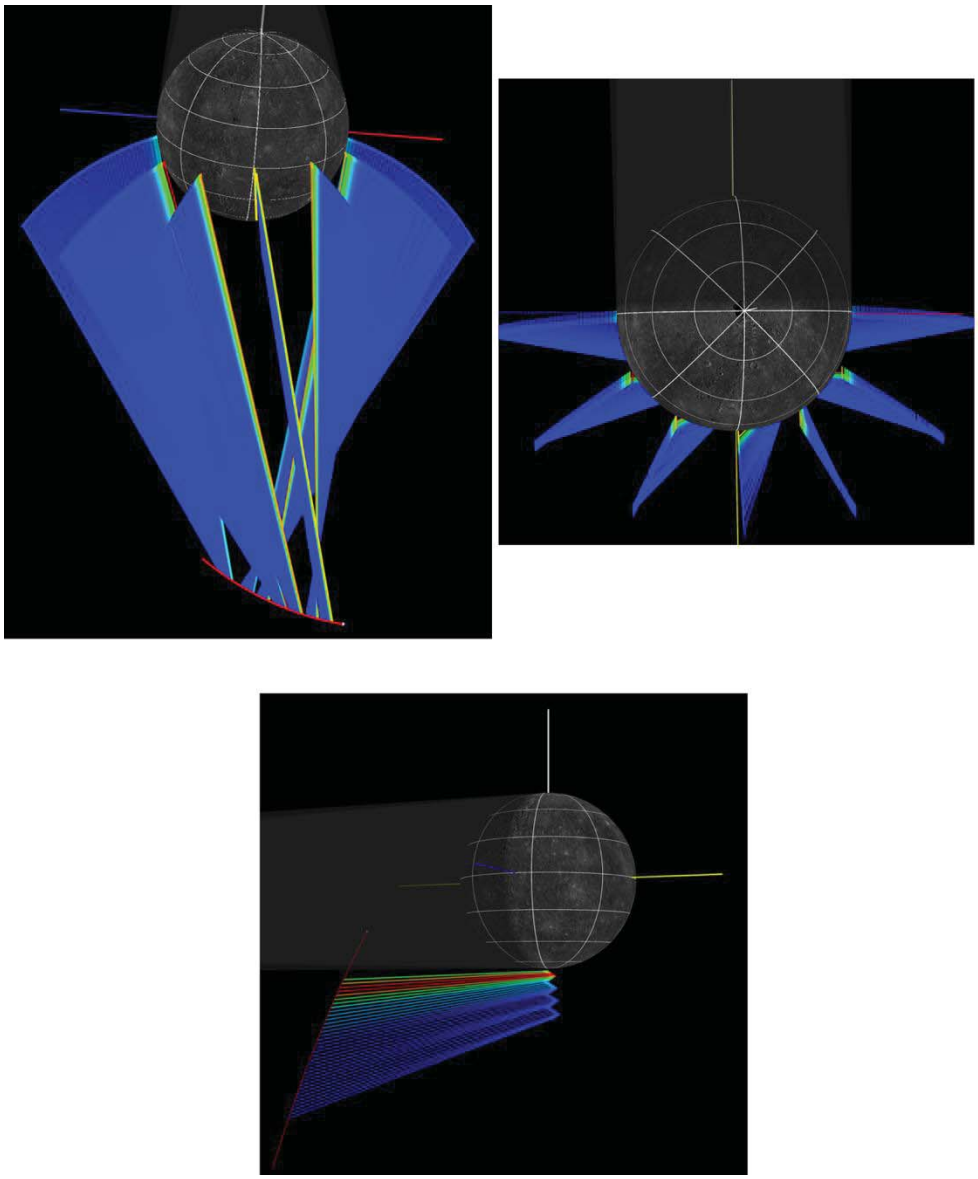

Fig. 2. Examples of UVVS lines of sight for dayside limb scans from two perspectives (top) and a south pole limb scan (bottom). The spacecraft orbit is indicated by the curved red line. The white, blue, red, and yellow lines indicate Mercury's rotation axis, dawn, dusk, and the subsolar point, respectively. Shaded colors indicate sodium emission radiance, which increases linearly from blue to red.

The other type of observation described in this paper is a south pole limb scan. An example is shown at the bottom of Fig. 2**.** These are altitude profiles above the south pole that can only be obtained during part of Mercury's year. In

these observations the UVVS is scanned back and forth above the south pole terminator. Similar observations are not possible at the north pole because MESSENGER's eccentric orbit has its periapse at high northern latitudes. The spatial coverage, in latitude and local time, of both limb scan types is shown in Fig. 3. The limb scans primarily probe the low-latitude dayside in contrast to ground-based observations that typically include Mercury's entire disk as seen from Earth.

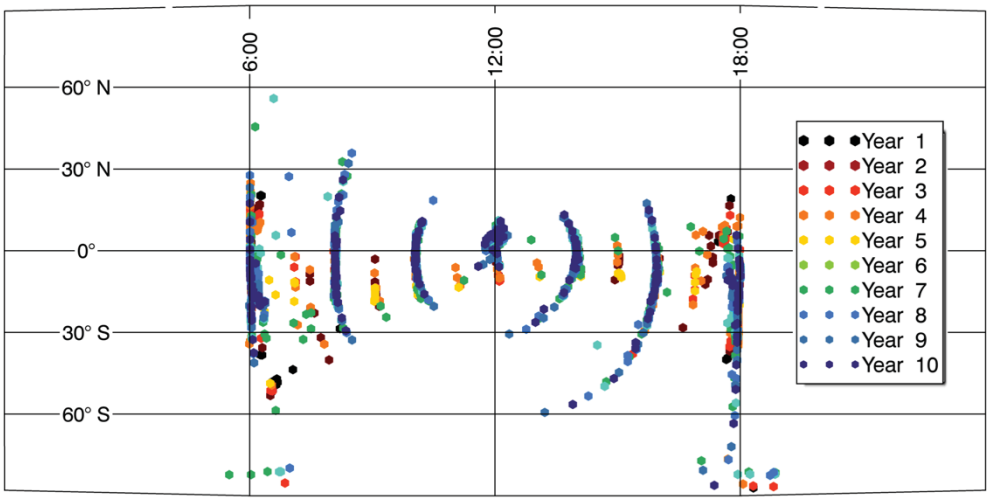

Fig. 3. UVVS limb scan coverage. Each point indicates the local time and latitude of a limb scan's tangent point at its lowest tangent altitude. Each symbol color represents a different Mercury year during MESSENGER's orbital mission.

2.2. Qualitative Interpretation of Limb Scan Data

In this section we describe some general features of the dayside and south

pole limb scans. Examples of UVVS dayside and south pole limb scans are shown in Fig. 4, which shows the observed sodium radiance (sum of D_1 and D_2 emission lines) above Mercury's limb as a function of line-of-sight tangent altitude. The limb scans show a two-temperature structure, which is apparent in Fig. 4 at 6, 12, and 16 h local time by a sharp change in slope between 500 and 1500 km. The cooler component has a steeper slope and is closer to the surface. It comprises the bulk of the exosphere observed by dayside limb scans. The energetic component has a relatively shallow slope, is relatively tenuous, and has been detected by UVVS up to 4000 km above the dayside surface.

Limb scan observations have been conducted regularly throughout the mission and provide consistent observing geometry, allowing us to search for year-to-year variations in emission. The observations shown in Fig. 4 are very similar from one Mercury year to the next, especially for the near-surface (cooler) component of the exosphere. We do show an example (Fig. 4, 12h local time) where there is evidence of year-to-year variability above ~700 km altitude. However, because the signal-to-noise level is low in these observations, as indicated by the large error bars in Fig. 4**,** this variability has yet to be confirmed as real.

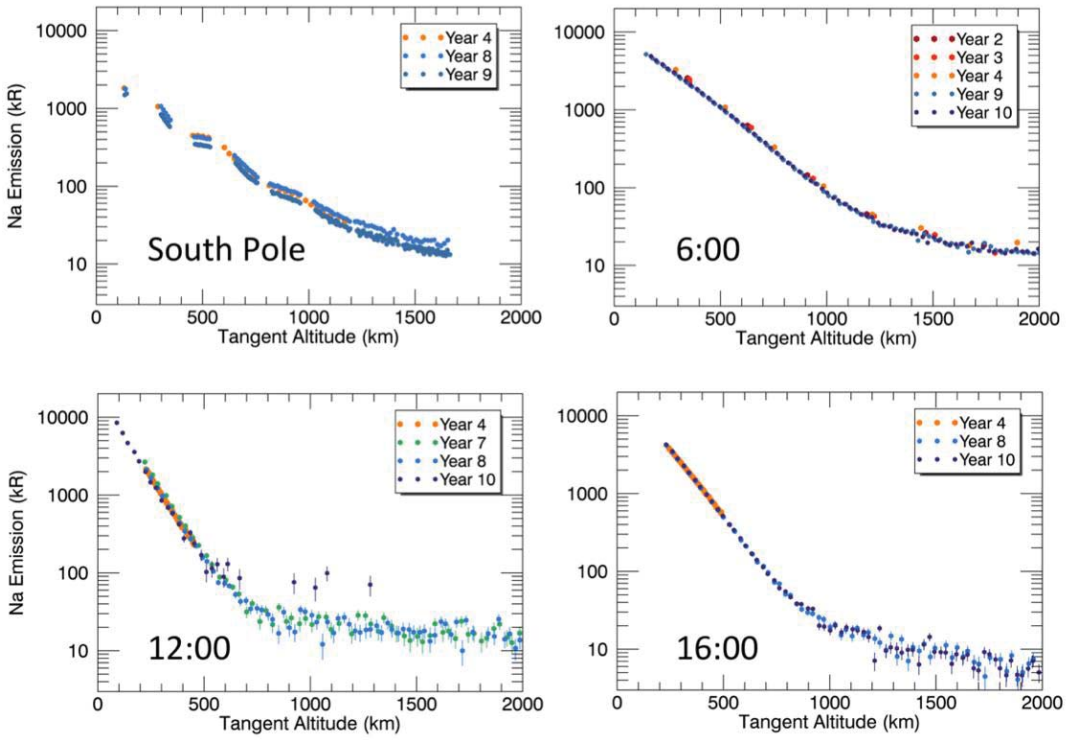

Fig. 4. Examples of UVVS altitude profiles (limb scans). Each symbol color represents a different Mercury year during MESSENGER's orbital mission. The upper left panel shows south pole limb scans. The panels labeled by local time show dayside limb scans taken at low latitudes. Each panel shows data from a short range of true anomaly angles: between 10° and 15° for the south pole plot and between 65° and 70° for the rest. Uncertainties were calculated from the SNR obtained during data processing. The gaps in the south pole scans are explained in a footnote.[1]

This year-to-year repeatability is surprising given the short-term episodic variability reported by ground-based observers. For example, Killen et al. (2001) reported a factor of three increase in total exospheric content over

[1] The gaps in the south pole scans shown in Fig. 4 are due to the unusual observation geometry shown in the bottom panel of Fig. 2 at which they were acquired. For those scans the UVVS line of sight is swept back and forth across the south polar terminator. We filtered those scans to include a short range of local times, resulting in data gaps near the surface.

several days. Leblanc et al. (2009) also reported changes in exospheric emission, both in brightness and spatial pattern, over a single Earth day. Mangano et al. (2013) observed changes on the order of hours. The repeatability observed by UVVS is also surprising in light of Monte Carlo exosphere simulations that populate the exosphere with episodic processes such as sputtering and ion-enhanced diffusion (e.g., Leblanc and Johnson, 2010; Wang and Ip, 2011).

It is possible that our observation geometry makes it difficult to detect episodic variability in our dataset. One reason might be the limited spatial coverage of UVVS as shown in Fig. 3. For example the rapid variability seen by Leblanc et al. (2009) was particularly strong over the mid-latitude regions that we cannot observe on a routine basis with limb scans, and which may receive the highest ion fluxes (Sarantos et al., 2007; Benna et al. 2010). Still, our observations do include areas in the southern hemisphere (Fig. 4) bombarded by ions (Winslow et al., 2012).

Sprague et al. (1997, 1998) suggested that sodium emissions in ground-based data were associated with geological features. In contrast, the year-to-year repeatability in Fig. 4 implies that geology does not strongly affect the exosphere. Because of Mercury's 3 : 2 orbital resonance (e.g., Zuber et al., 2007), the longitude at a given local time changes 180° from one year to the next, yet the UVVS observations of sodium emission do not change appreciably between successive Mercury years. However, the emissions that Sprague et al. (1997, 1998) associated with geological features were at middle latitudes with poor limb scan coverage.

Although many observers and modelers have emphasized episodic variability, some have studied the exosphere's seasonal variability. Potter and Morgan (1987) presented the first evidence for this seasonal variation by showing a correlation between sodium column density and radiation acceleration, the seasonally variable acceleration experienced by sodium atoms due to solar photon scattering. This repeatability is also evident in the plots of Potter et al., 2007, Leblanc and Johnson (2010), and Wang and Ip (2011).

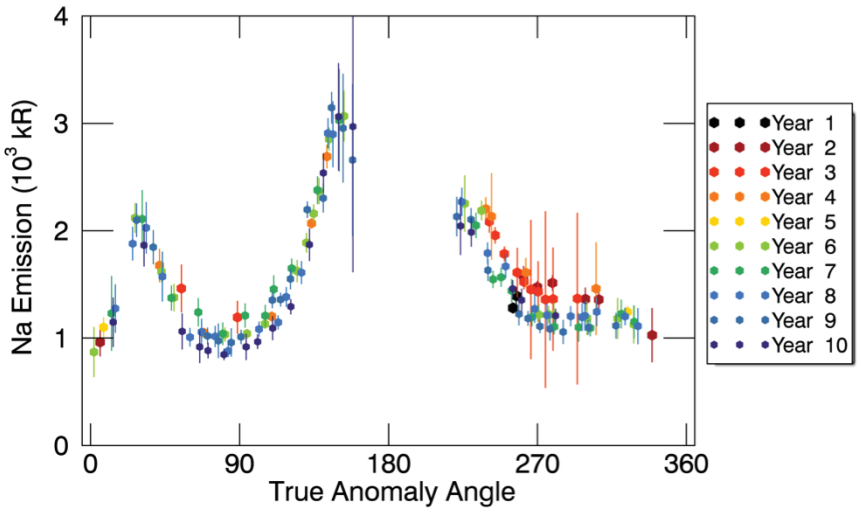

Fig. 5. Seasonal pattern of sodium emissions near the subsolar point, illustrated by the limb-scan radiance at 300 km altitude. Each symbol color represents a different Mercury year during MESSENGER's orbital mission. As a result of variable altitude sampling, the radiance at that altitude was interpolated from observations at nearby altitudes in each scan using the fits to the data described in Section 3.2; the uncertainties are due to this interpolation. The gap in observations near aphelion (180° true anomaly) is due to restrictions on observation geometry.

The seasonal pattern in sodium emissions observed by UVVS is shown in Fig. 5. We chose to plot emissions near the subsolar point at a tangent altitude of 300 km because there are many observations at this altitude throughout the

mission. The pattern is quite different from the ground-based observations referenced above, which show a minimum in emission near aphelion (true anomaly angle of 180°), where we see a maximum in emission. However the ground-based seasonal pattern cannot be compared directly with Fig. 5. The seasonal pattern reported by the ground-based observers referenced above is for disk-integrated emissions, while Fig. 5 is for the subsolar point only.

3. Quantitative interpretation of limb scans

Limb scans provide ideal data for estimating exospheric temperature and density. To make such estimates we adapt expressions from Chamberlain (1963) for line-of-sight column density as a function of tangent altitude given two parameters: surface density n_o and temperature T. We fit these expressions to the near-surface dayside UVVS observations, as shown in Fig. 6. Chamberlain's expressions rest on a number of assumptions that we discuss below.

3.1. Estimating line-of-sight column density

The first step, converting the UVVS emission radiance to line-of-sight column density N (cm^{-2}), uses the formula

$$N = 10^9 \, 4\pi I / g \qquad (1)$$

where $4\pi I$ is the radiance in kR. The g-value (g) is the rate (s^{-1}) at which a sodium atom scatters solar photons in the D_1 and D_2 lines. It depends on the

distance from, and radial velocity relative to, the Sun (Smyth, 1986; Killen et al., 2009). For this paper, we assume that the sodium atoms are nearly at rest with respect to Mercury. This assumption requires justification because sodium atoms have a distribution of radial velocities and experience substantial anti-sunward acceleration due to radiation acceleration, which can be up to half of Mercury's surface gravitational acceleration (Smyth, 1986; Ip, 1986).

We tested and confirmed this assumption with a Monte Carlo model (Burger et al., 2010, 2012) that calculates the *g*-value for each simulated sodium atom separately. This analysis is presented in Appendix 1. Our testing shows that the approximation introduces minimal error due to the modest speed of most sodium atoms relative to Mercury (excluding some portions of the exosphere not considered in this paper). This assumption holds despite the strong forces experienced by sodium atoms, as applying a force to a gas does not necessarily change its speed distribution. This fact is counterintuitive, but Feynman (1963) showed, for the simplified case of a plane-parallel exosphere, that the speed distribution is independent of height despite gravitational acceleration (see also Johnson, 1990). Adding radiation acceleration does not necessarily change this result. Feynman (1963) mentioned that a height-independent speed distribution applies to any gas in a conservative potential, and Bishop and Chamberlain (1989) showed that the addition of (speed-independent) radiation acceleration to gravitational acceleration results in a conservative potential.

These results do not strictly apply to Mercury's exosphere for several reasons. One is that the radiation acceleration is speed dependent (Killen et al.,

2009), meaning that the sodium atoms are not in a conservative potential. Another is that sodium atoms have fairly short photoionization lifetimes, resulting in losses not accounted for by the methodology of Chamberlain (1963). Finally, Chamberlain (1963) showed that the speed distribution does change with altitude, unlike Feynman's example of a plane-parallel exosphere. Despite these caveats our testing shows that the constant *g*-value approximation is adequate for the dayside sodium exosphere. We do, however, have UVVS observations for which this approximation would clearly fail, such as in Mercury's sodium tail, whose atoms are moving anti-sunward at many kilometers per second (Ip, 1986; Mura et al., 2009), or for a gas with thermal energy close to escape energy, such as Mercury's calcium exosphere (Burger et al., 2012).

3.2. Deriving temperature and density from limb scans

The line-of-sight column density N from Eq. (1) is related to the density through

$$N = 2KHn \qquad (2)$$

where n is the density of the exosphere at the line-of-sight tangent point, H is the scale height of the exosphere, and $2K$ is the ratio between the line-of-sight column density tangent to the surface and the vertical column density ($\sim Hn$). $2K$ is approximately $(2\pi r/H)^{1/2}$ (Chamberlain, 1963). The scale height is discussed in more detail in Section 4.2. This approximation breaks down as the altitude

increases or as temperature increases. It also assumes that the exosphere is spherically symmetric, which it is not. Practically speaking, however, any tangent line of sight will only sample a small portion of the exosphere.

In Chamberlain's methodology the density n as a function of altitude is approximated by

$$n = \zeta\, n_0\, e^{-(U-U_0)/kT} \qquad (3)$$

where U is the gravitational potential energy, T the temperature, n_0 the surface density, and U_0 is the gravitational potential energy at the surface. The factor ζ (≤1), from Chamberlain (1963), accounts for the fraction of the initial isotropic Maxwellian distribution that is actually present at a given altitude, subject to conservation of energy and angular momentum. Most sodium atoms in Mercury's exosphere are on ballistic orbits for which the only restrictions are that the total energy is negative, and orbits must intersect the exobase. We assume ζ=1, (no dynamical restrictions) as appropriate for a cool gas deep within a gravitational well.[2] The limitations of Chamberlain's approach are that there are no loss processes and that the speed distribution of particles leaving the exobase is assumed to be a Maxwell flux distribution. It also assumes that the exosphere is spherically symmetric while the actual exosphere is non-uniform. However, our analysis does not assume that the exosphere is uniform, it only assumes that exosphere varies more rapidly in the radial direction than in the longitudinal/latitudinal directions so that the non-uniformity of the

[2] The approximation is valid to an altitude of approximately 1000 km for sodium at 1200 K (Chamberlain and Hunten, 1987, Appendix IX).

exosphere does not strongly affect the results. We believe this is reasonable for the sodium exosphere, given its small scale height (Section 4.2).

We modified the potential energy U in Eq. (3) to include radiation acceleration. Following Bishop and Chamberlain (1989) the potential energy for the combination of gravity and radiation acceleration is written as

$$U = -GMm/r + mbr\cos(\vartheta) \quad (4)$$

where b is the photon acceleration from Wang and Ip (2011), ϑ is the solar zenith angle (the angle between the local radial vector and the Mercury-Sun axis), G is the gravitational constant, M is the mass of Mercury, m is the mass of a sodium atom, and r is the distance from Mercury's center.

We fit Eqs. (2)–(4) to limb scan data in order to estimate the temperature and surface density of the sodium exosphere. Example fits are shown in Fig. 6. We used a non-linear least squares fitting routine (Markwardt, 2009), which adjusted surface density and temperature to find the best fit. Because Eqs. (1)-(4) are approximate, we tested the fitting routine with the Monte Carlo model as described in Appendix 1.

The columns near the surface are sometimes optically thick, which complicates Eq. (1) because some of the photons emitted by sodium atoms are scattered before reaching UVVS. For this reason we label the y-axis of Fig. 6 the apparent column density. This scattering causes the slight turndown in the data at the lowest altitudes shown in Fig. 6. We typically see this behavior for line-of-sight columns above $\sim 1\times10^{11}$ cm^{-2}. To match the data better at low tangent altitudes and moderate optical depths we provide a correction to account for

these scattered photons. The details of this correction are described in Appendix 2. Both uncorrected and corrected fits are shown in all panels of Fig. 6 to illustrate the need for this optical depth correction.

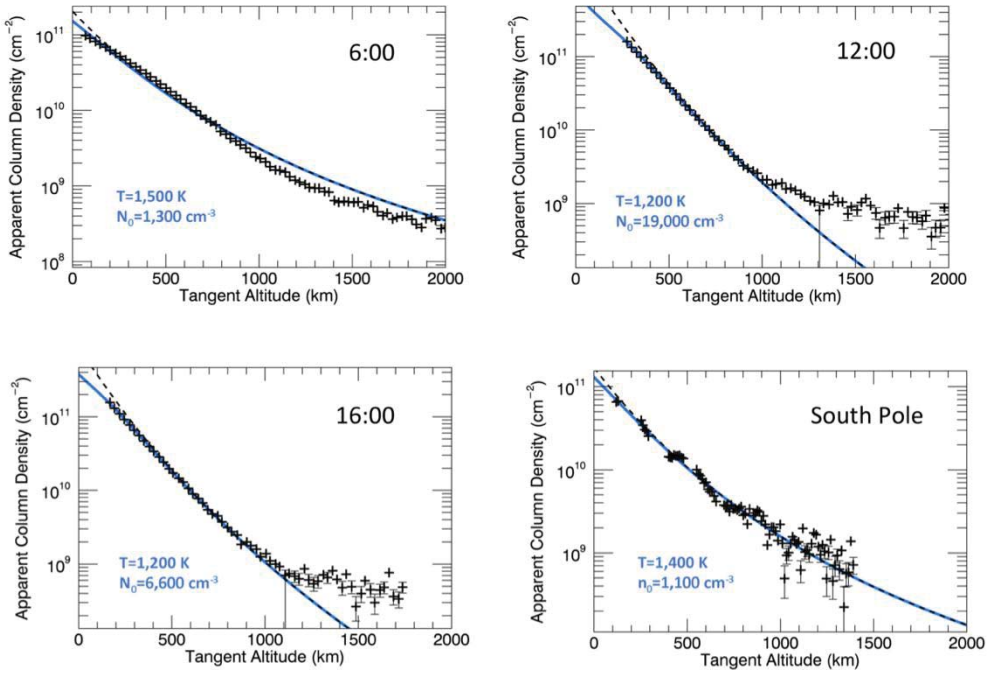

Fig. 6. Examples of fits to dayside limb scans (local times indicated) and the south pole. Data are represented by crosses, and the model is shown by a black dashed line. The blue line is the model with the optical depth correction. The resulting temperature and surface density used for the fits are indicated by blue text. Observations were taken on 6 June 2012, except for the south pole observation, which took place on 17 October, 2011.

Despite having only two free parameters, these expressions provide exceptional fits to the low-altitude, low-temperature portion of the limb scans (Fig. 6). The fits at 12:00 and 16:00 pass through nearly every data point below ~1000 km, whereas at dawn (6:00) and the south pole, the fits capture the general trend of the limb scan but do not match every point. We also tried

similar fitting procedures for the more energetic component of the exosphere observed at high tangent altitudes, but we were unable to constrain its temperature. The problem may be due to the low signal to noise ratio of the data or to the inherent limits of our simple physical model.

4. Results

4.1. Temperature

The estimated temperature exosphere near the subsolar point is shown as a function of Mercury true anomaly in Fig. 7. This is the temperature for the cooler, near-surface portion of the exosphere identified in Section 2. After correcting for the effects of radiation pressure and optical depth, the estimated temperature is approximately constant at ~1200 K over the Mercury year and consistently so over MESSENGER's first 10 Mercury years of orbital data. The error bars in Fig. 7 are derived from the covariance matrix calculated by the fitting routine. These are generally quite small because of the quality of the fits and large number of data points.

The same is true for all low-latitude dayside limb scans, though dawn, dusk, and the south pole, are slightly warmer at ~1500 K (as demonstrated in the fits in Fig. 6). The average temperature of the low-latitude dayside limb scan fits away from the terminator was 1150 K with a standard deviation of 50 K. The average temperature of the terminator (dawn, dusk, and south pole) limb scan

fits was 1450 K with a standard deviation of 130 K. This large standard deviation is reflective of the relatively poor fits of the limb scans taken near the terminator.

The estimated temperature is consistent with some, but not all, previous ground-based measurements. Potter and Morgan (1987) made the first temperature estimate by measuring the Doppler-broadened emission line width and concluded that the sodium was near Mercury's surface temperature. They did not make an estimate of the temperature, but demonstrated that a simulated 500 K line profile was a much better match than 5000 K. Killen et al. (1999) used ultra-high resolution line profiles obtained at the Anglo-Australian telescope to derive temperatures of 1500 K for the central disk and a combination of 750K and 1500 K sodium at the poles. They ruled out a high temperature component (>5000 K). Schleicher et al. (2004), Leblanc et al. (2009), and Leblanc et al. (2013) found much higher temperatures, on the order of 3000 K, using similar measurements but at lower spectral resolution. In addition to Doppler broadening, the line profiles also usually indicate anti-sunward motion. Leblanc et al. (2009), Potter et al. (2009), Potter et al. (2013), and Leblanc et al. (2013) estimated the anti-sunward motion at around 1 km s^{-1} or less on the disk. UVVS cannot measure the emission line width or bulk velocity because it has insufficient spectral resolution.

Our temperature estimate is approximately consistent with those estimated from exospheric altitude profiles obtained by Potter et al. (2013) during Mercury's solar transits. Potter et al. (2013) used Chamberlain's (1963)

expressions to estimate temperatures around the terminator (the only portion of the exosphere visible during the transit). Their estimates were similar, on average, to our estimates at the terminator (dawn, dusk, and the south pole), but with a wider range of values (800-3000 K). They also identified a possible energetic component at high altitudes. Schleicher et al. (2004) measured scale heights, an indirect measure of temperature (see Section 4.2), during another solar transit and found values similar to ours (Fig. 10).

The energy distribution of exospheric particles provides a strong constraint on source processes. Our estimated temperature for the cooler component seen in the limb scans, 1200-1500 K, is consistent with the typical energies of sodium atoms ejected by photon-stimulated desorption (PSD). This agreement suggests that PSD is the dominant source process for this cooler component, as other ejection mechanisms have quite different energy distributions. Measurements of the PSD energy distribution were described by Yakshinskiy and Madey (1999, 2004) and summarized by Schmidt et al. (2012, 2013). Measured energy distributions vary with substrate. For example, we found that the measured PSD energy distribution from an SiO_2 substrate (Yakshinskiy and Madey, 1999) is well fit by a 900 K Maxwell flux distribution, while experiments using a lunar sample (Yakshinskiy and Madey, 2004) or water ice (Johnson et al., 2002) found distinctly non-Maxwellian energy distributions with similar average ejection energies.

By contrast, thermally desorbed or partially thermalized sodium would be closer to Mercury's surface temperature, which ranges from ~100 to ~700 K

(Yan et al., 2006). Impact vaporization is expected to produce much warmer sodium, at 2000–5000 K (Cintala, 1992). Ion sputtering is much more energetic and produces a non-Maxwellian energy distribution (e.g., Johnson, 1990). The latter two may contribute to the tenuous high-energy sodium we see at high altitudes (Fig. 4).

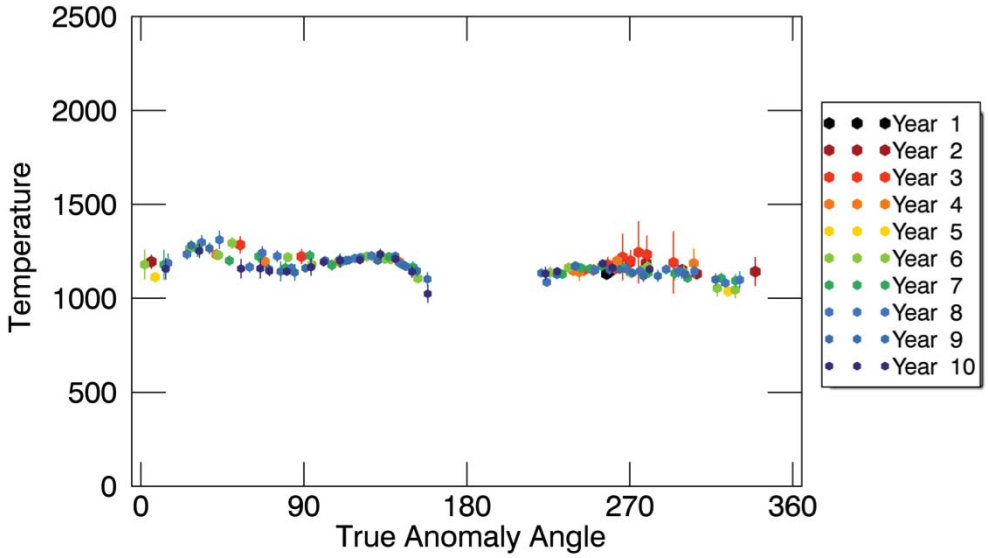

Fig. 7. Estimated sodium exosphere temperature as a function true anomaly for dayside limb scans near the subsolar point. Each point is from a fit to a single limb scan. This is the temperature of the near-surface part of the exosphere identified earlier.

Because thermalization, the thermal equilibration of atoms with a surface, is seen in laboratory experiments (e.g., Yakshinskiy and Madey, 2005) and is also a common assumption in Monte Carlo models (e.g., Smyth and Marconi, 1995; Mura et al., 2009; Leblanc and Johnson, 2010), we searched our data for a colder component. Detecting sodium at the surface temperature is difficult for limb scans because such cold sodium would be confined within 100 km of the surface where we have limited high resolution observations, but we can place upper

limits on the presence of a surface-temperature component.

A demonstration of what a limb scan would look like with the addition of a thermalized component is given in Fig. 8 for two different local times: early morning, during which thermal desorption might release sodium atoms adsorbed on the nightside (e.g., Sprague et al., 1997), and the subsolar point, where the surface is warmest. We used Eqs. (2)-(4) to add a surface-temperature component to the fitted model, giving it the same vertical column density as the warmer component. The surface temperature used is typical for that local time (Yan et al., 2006). The left panel (early morning) shows that an abundant thermalized component would be obvious, but we do not see one in the data. At the subsolar point (right panel), the difference is much more subtle. Though we cannot rule out the presence of a thermal component, we can say that it is much less abundant than the ~1200 K component in the dayside limb scans.

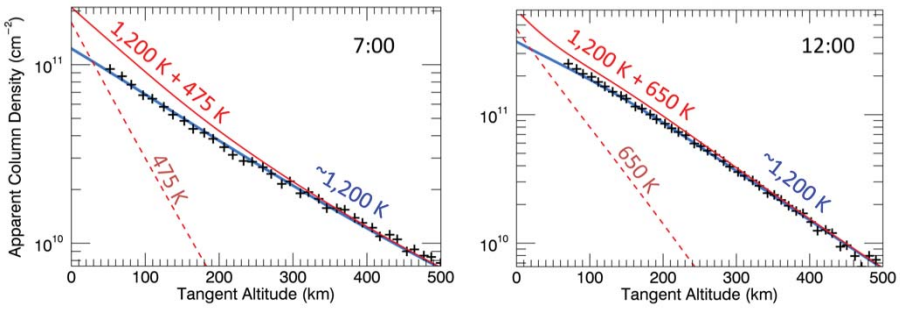

Fig. 8. Example of a search for a surface-temperature component at early morning ("7:00") and the subsolar point ("12:00"). The solid red line shows a surface-temperature component added to the observed 1200 K component. For this example it was assumed that the surface-temperature component has the same vertical column density as the 1200 K component. These observations were taken on 29 October, 2012.

Yakshinskiy et al. (2000) provided a possible explanation for the absence of a thermal component: space weathering may inhibit thermal desorption. They found that it took substantially higher temperatures to desorb sodium from an ion-irradiated substrate as compared to a non-irradiated substrate (see also Domingue et al., 2007) in a temperature-programmed desorption experiment. Temperature-programmed desorption is described, e.g., in Oura et al. (2003). Using data from that experiment we estimate that the binding energy of sodium to the irradiated substrate is higher, about 2.5 eV, larger than typically assumed in Monte Carlo models, a range of values centered on 1.85 eV (Leblanc and Johnson, 2003, 2010; Mura et al., 2009). That higher binding energy results in a very low thermal desorption rate, only about 10^{-5} s^{-1} even at Mercury's highest surface temperature. This rate means that a sodium atom adsorbed at 700 K would spend about 10^{5} s on the surface before desorbing. This value contrasts with theoretical estimates by Hunten et al. (1988) of $\sim 10^{-11}$ s. PSD is about an order of magnitude faster than this new estimate of the adsorption time, on the basis of the PSD cross sections in Yakshinskiy and Madey (1999), and similar in magnitude to the first estimate by McGrath et al. (1986).

These numbers are highly uncertain given that Mercury's surface composition is unlike the substrates used in those experiments (Evans et al., 2012), but they provide a possible explanation for the dominance of the 1200 K component: sodium atoms adsorbed on the surface are photo-desorbed before being thermally desorbed, a process that could repeat itself dozens of times

during their photoionization lifetimes. Another possibility is low accommodation. In that scenario the atoms do not stick when they return to the surface, but rather they scatter off of the surface with reduced energy. Full accommodation would result in a surface-temperature exosphere, whereas no accommodation is equivalent to an elastic collision. Some sodium exosphere modelers (Burger et al., 2010; Mouawad et al., 2011, Wang and Ip, 2011) concluded that low accommodation is necessary to match their observations, and such low accommodation might explain the lack of a thermalized component in Fig. 8. Accommodation is discussed further in Appendix 1.

Monte Carlo modelers have long populated the exosphere with diverse and variable source processes, each with a signature speed distribution ranging from surface temperature to non-thermal sputtering. However the nearly constant temperature shown in Fig. 7 suggests that, excluding the tenuous energetic component, the exosphere observed by these limb scans (low latitude dayside and south pole), has a single temperature that does not vary much with true anomaly. We considered the possibility that this near-surface portion of the exosphere is a mixture of several temperature components, but adding additional components only made the fits worse, as demonstrated in Fig. 8.

It is, however, possible to fit a limb scan with a mixture of source processes and thermal accommodation, as Wang and Ip (2011) did with UVVS polar limb scans taken during one of MESSENGER's Mercury flybys (Vervack et al., 2010). Those observations were similar to the south polar, dawn, and dusk scans shown here (Fig. 6), which we fit with a single temperature component (~1500

K). Wang and Ip (2011) used 4 source processes. Such a scenario is unlikely to produce an exosphere that can be fit by a single temperature model. Each source process used by Wang and Ip (2011) has a different seasonal variation so that the temperature should change throughout the Mercury year. Further, at least two out those 4 of were episodic processes (sputtering and ion-enhanced diffusion) that would not show the year-to-year repeatability evident in Fig. 4.

Though the bulk of the exosphere observed by limb scans appears to be supplied by a single process, PSD, other space-weathering processes must contribute to exosphere indirectly. PSD would quickly deplete any surface layer of sodium, so sodium must be replenished by processes such as thermal diffusion from regolith grain interiors, and the grains themselves must be replenished by gardening to maintain the exosphere over the long term (Killen et al., 2004). Though we do not see the sporadic sources of sodium expected from magnetospheric processes, ion precipitation may help sodium diffuse to out of grains, especially where the surface is relatively cold (Sarantos et al., 2008, 2010; Burger et al., 2010). Further, an exospheric source proportional to solar photon flux would peak at the subsolar point, which we do not observe (Fig. 6).

We were not able to constrain the energy distribution of the high-altitude hot component. Fitting those data with Eqs. (2)-(4) resulted in a wide range of temperatures. If this population is the same as that supplying Mercury's sodium tail, then its energy distribution was constrained by Burger et al. (2010) and Schmidt et al. (2012). Both concluded that the tail is primarily populated by the

high-energy portion of the PSD energy distribution described by Johnson et al. (2002) and Wurz et al., (2010).

4.2. Scale height: Radiation pressure compression of the exosphere

The UVVS limb scan data illustrate that Mercury's dayside exosphere is compressed by radiation acceleration. The scale height used in the expressions from Section 3.2 is given by

$$H = n/(\mathrm{d}n/\mathrm{d}r) = kT/(\,GMm/r^2 + mb\cos(\vartheta)\,). \qquad (5)$$

where the parenthetical expression in the denominator is a sum of two terms, the gravitational acceleration and the radial component of the radiation acceleration b. This latter term reduces the scale height; according to Eq. (5) the dayside exosphere should be compressed by radiation acceleration, and in fact we do see this effect in both the Monte Carlo simulations and UVVS observations. Fig. 9 shows two limb scans taken during high and low radiation acceleration. The limb scan taken during high radiation acceleration has a scale height about 30% smaller than the low radiation acceleration case. For each, the fit to Eq. (2) gives approximately the same temperature.

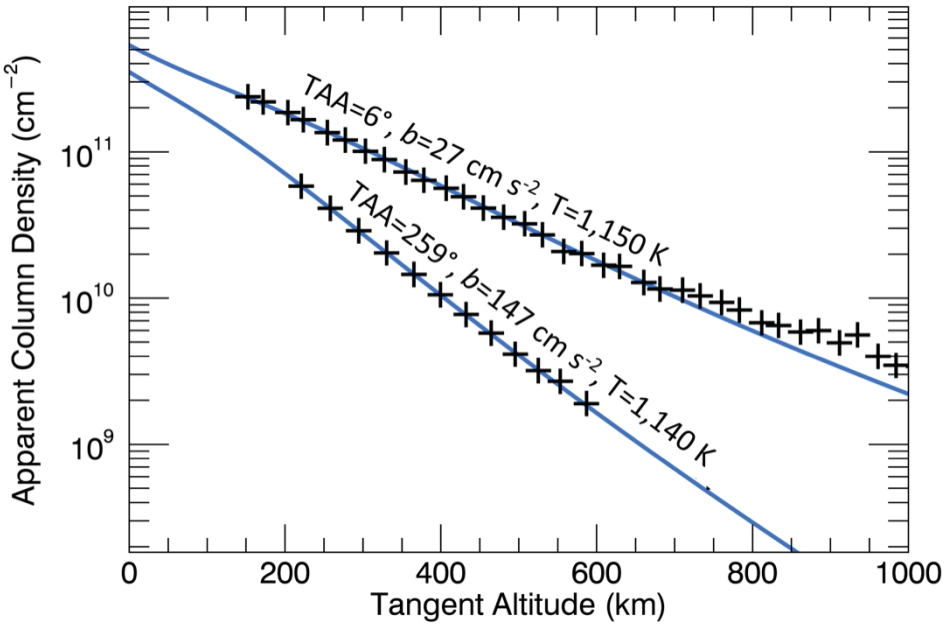

Fig. 9. Two different noon limb scans taken with different values of radiation acceleration. They have similar temperatures but different scale heights because of radiation acceleration, which compresses the exosphere. The fit for each limb scan is shown in blue. The low-photon acceleration example was observed on 24 May 2011, the other on 13 June 2011.

Estimated scale heights near the surface and radiation acceleration are compared as functions of Mercury true anomaly in Fig. 10. The mean value of the scale height is near 90 km, but there is a clear seasonal pattern. The exospheric scale height is smallest when radiation acceleration is largest. Scale heights are normally directly proportional to temperature, but here we have a different system in which the scale height changes while the source temperature remains approximately constant (Fig. 7). As described in section 3.2 and Appendix 1, there were many approximations that went into the equations used to fit the limb scans, but this agreement between the predicted and measured scale heights suggest that the approximations were valid.

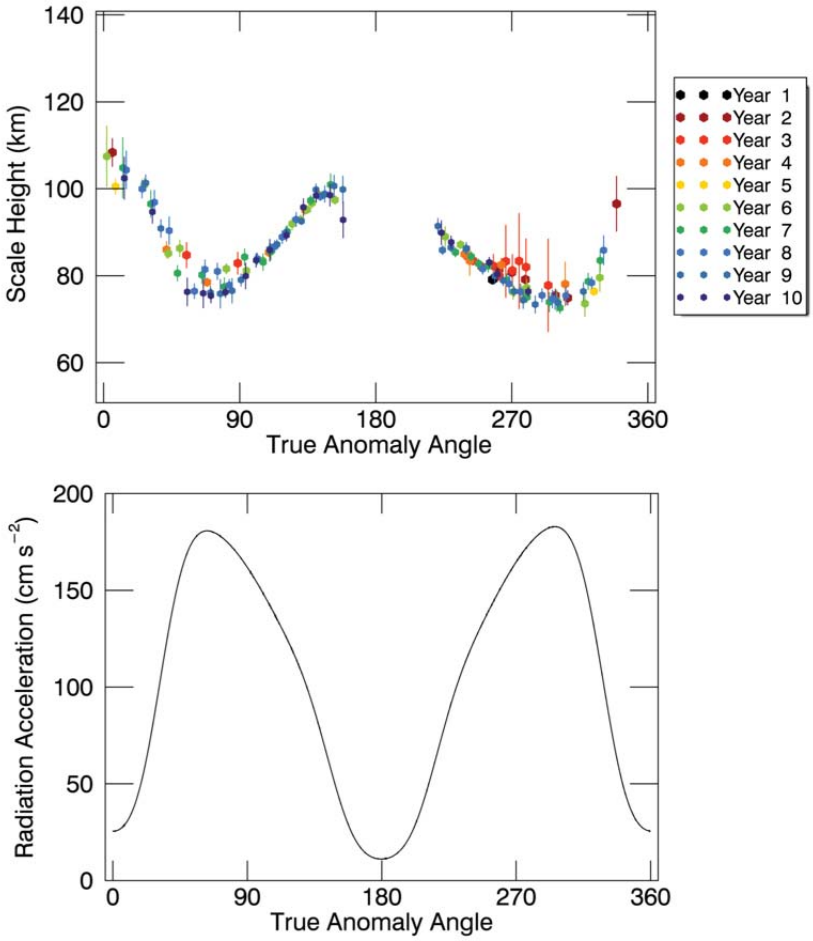

Fig. 10. (Top) Exosphere scale height as a function of true anomaly angle near the subsolar point. (Bottom) Radiation acceleration for a sodium atom at rest relative to Mercury as a function of true anomaly.

4.3. Density

The estimated near-surface densities have a complex pattern, one that depends on true anomaly, local time, and latitude. In general, the near-surface density is largest on the dayside away from the terminator and it peaks near aphelion, when radiation acceleration and photoionization are at their lowest.

Near-surface densities on the dayside range from $\sim 10^3$ cm^{-3} to $\sim 10^5$ cm^{-3}, and those near the terminator ranged from $\sim 10^2$ cm^{-3} to $\sim 10^4$ cm^{-3}.

Estimated near-surface densities are shown as a function of Mercury true anomaly near the subsolar point in Fig. 11. As with sodium emission (Fig. 5) and temperature (Fig. 7), there is a seasonal pattern that is unchanging from one Mercury year to the next. As with the plot of emission (Fig. 5), this pattern is difficult to compare with ground-based observations and models. There is no published estimate of density at a specific local time as a function of true anomaly.

As with the temperature, the uncertainties come from the non-linear fitting routine and are quite small because of the good fits obtained with Eqs. (2)-(4).[3] However, these uncertainties do not account for systematic errors. Potter et al. (2007) described a possible systematic uncertainty. They concluded, contrary to our analysis in Appendix 1, that radiation acceleration changes the *g*-value markedly ($\sim \pm 50\%$) because of anti-sunward acceleration. We have included a 50% scale bar in the upper left of the figure to show the magnitude of such a systematic uncertainty, which is clearly too small to account for the large seasonal changes in density seen in Fig. 11.

[3] Several data points have large uncertainties. These are fits to limb scans with relatively few data points from early in the mission. The use of only a few data points in the fitting routine resulted in large uncertainties.

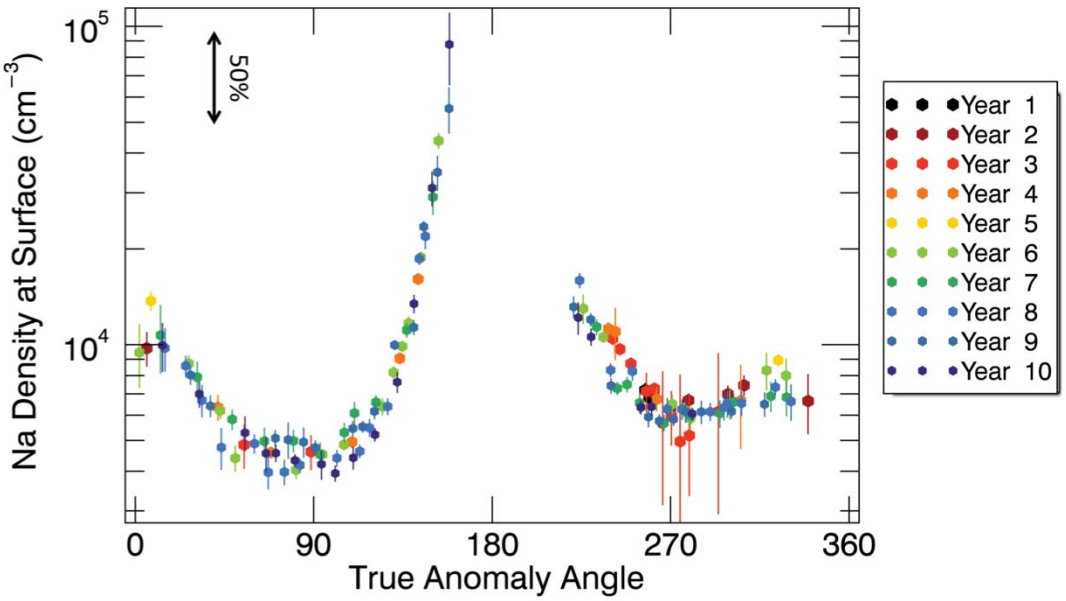

Fig. 11. Surface sodium density estimated from observations taken near the subsolar point is shown as a function of true anomaly angle. The arrow at the upper left shows the magnitude of a 50% systematic uncertainty (see text).

Although PSD alone may be responsible for the ejection of most sodium in exosphere, other physical processes must be involved as described above. If the exospheric source rate were only dependent on solar photon flux then there would not be a peak in the exospheric density near aphelion. Instead a mix of transport, source, and loss processes determines exospheric behavior. Leblanc and Johnson (2003), for example, suggested that the sodium source rate might peak at aphelion because the terminator rotates fastest at that time, causing rapid ejection of sodium adsorbed on the nightside surface. Photon pressure is also at a minimum during aphelion (with another, smaller minimum at perihelion), during which anti-sunward transport is minimized (Potter et al., 2006). This could also contribute to a subsolar peak near aphelion. The

interplay of source, loss, and transport processes will likely require detailed numerical modeling in order to explain the trends in Fig. 11 and elsewhere in the exosphere.

5. Conclusion

We report the first orbital observations of Mercury's sodium exosphere. These observations provide unprecedented coverage in both local time and true anomaly, though with less geographical coverage than that of ground-based observations; the limb scans described here were taken mostly at low latitudes and directly above the south pole (Fig. 3). The observations show year-to-year repeatability: at a given local time and true anomaly the emissions are nearly identical from one Mercury year to the next.

We interpreted the UVVS limb scan data with a simple model to estimate the temperature and density of the near-surface exosphere (within about 500–1500 km of the surface). The model accounts for the effects of radiation acceleration and photon scattering. We found a temperature of about 1200 K, suggesting that photon-stimulated desorption is the primary source process. A high-energy process is also present and may be episodically variable. That process could the energetic tail of the PSD energy distribution, impact vaporization, or sputtering. There is no indication in these data of thermal desorption or thermalization (accommodation) of the exosphere to the local surface temperature.

These conclusions are surprising in light of the previous literature, which has suggested that sodium is ejected from the surface by a complex mixture of episodic processes. Though aspects of these results have been reported earlier, the robust nature of the year-to-year repeatability and nearly constant near-surface exospheric temperature were unexpected. Although a direct comparison with ground-based observations is beyond the scope of this work, ground-based data should be re-evaluated in the context of year-to-year repeatability.

Acknowledgements

The visualization of UVVS observations shown in Fig. 1 was developed at the Laboratory for Atmospheric and Space Physics by Jay Kominek, Ken Griest, and Dane Larsen. The MESSENGER project is supported by the NASA Discovery Program under contracts NAS5-97271 to The Johns Hopkins University Applied Physics Laboratory and NASW-00002 to the Carnegie Institution of Washington. RJV and RMK are supported by the MESSENGER Participating Scientist Program

References

Baumgardner, J., Wilson, J.K., Mendillo, M., 2008. Imaging the sources and full extent of the sodium tail of the planet Mercury. Geophys.Res.Lett. 35, L03201. doi:10.1029/2007GL032337

Benna, M., Anderson, B.J., Baker, D.N., Boardsen, S.A., Gloeckler, G., Gold, R.E., Ho, G.C., Killen, R.M., Korth, H., Krimigis, S.M., Purucker, M.E., McNutt Jr., R.L., Raines, J.M., McClintock, W.E., Sarantos, M., Slavin, J.A., Solomon, S.C., Zurbuchen, T.H., 2010. Modeling of the magnetosphere of Mercury at the time of the first MESSENGER flyby. Icarus 209, 3–10. doi:10.1016/j.icarus.2009.11.036

Bishop, J., Chamberlain, J.W., 1989. Radiation pressure dynamics in planetary exospheres: A “natural” framework. Icarus 81, 145–163. doi:10.1016/0019-1035(89)90131-0

Brown, R.A., Yung, Y.L., 1976. Io, its atmosphere and optical emissions, in: Gehrels, T., Matthews, M.S. (Eds.), Jupiter: Studies of the Interior, Atmosphere, Magnetosphere, and Satellites. Univ. Arizona Press, Tucson, p. 1102.

Burger, M.H., Killen, R.M., McClintock, W.E., Merkel, A.W., Vervack Jr., R.J., Cassidy, T.A., Sarantos, M., n.d. Seasonal Variations in Mercury’s Dayside Calcium Exosphere. Icarus. doi:10.1016/j.icarus.2014.04.049

Burger, M.H., Killen, R.M., McClintock, W.E., Vervack, R.J., Merkel, A.W., Sprague, A.L., Sarantos, M., 2012. Modeling MESSENGER observations of calcium in

Mercury's exosphere. J. Geophys. Res. 117, E00L11. doi:10.1029/2012JE004158

Burger, M.H., Killen, R.M., Vervack Jr., R.J., Bradley, E.T., McClintock, W.E., Sarantos, M., Benna, M., Mouawad, N., 2010. Monte Carlo modeling of sodium in Mercury's exosphere during the first two MESSENGER flybys. Icarus 209, 63–74. doi:10.1016/j.icarus.2010.05.007

Chamberlain, J.W., 1961. Physics of the Aurora and Airglow. Academic Press Inc., New York.

Chamberlain, J.W., 1963. Planetary coronae and atmospheric evaporation. Planet. Space Sci. 11, 901–960. doi:10.1016/0032-0633(63)90122-3

Chamberlain, J.W., Hunten, D.M., 1987. Theory of planetary atmospheres. An introduction to their physics andchemistry., International Geophysics Series, Vol. 36. Academic Press Inc., Orlando, FL, USA.

Chaufray, J.Y., Leblanc, F., 2013. Radiative transfer of emission lines with non-Maxwellian velocity distribution function: Application to Mercury D_2 sodium lines. Icarus 223, 975–985. doi:10.1016/j.icarus.2013.01.005

Cintala, M.J., 1992. Impact-induced thermal effects in the lunar and Mercurian regoliths. J. Geophys. Res. 97, 947–973. doi:10.1029/91JE02207

Domingue, D.L., Koehn, P.L., Killen, R.M., Sprague, A.L., Sarantos, M., Cheng, A.F., Bradley, E.T., McClintock, W.E., 2007. Mercury's Atmosphere: A Surface-Bounded Exosphere. Space Sci. Rev. 131, 161–186. doi:10.1007/s11214-007-9260-9

Evans, L.G., Peplowski, P.N., Rhodes, E.A., Lawrence, D.J., McCoy, T.J., Nittler, L.R.,

Solomon, S.C., Sprague, A.L., Stockstill-Cahill, K.R., Starr, R.D., Weider, S.Z., Boynton, W.V., Hamara, D.K., Goldsten, J.O., 2012. Major-element abundances on the surface of Mercury: Results from the MESSENGER Gamma-Ray Spectrometer. J. Geophys. Res. 117, E00L07. doi:10.1029/2012JE004178

Feynman, R.P., n.d. Volume 1, Chapter 40, in: Feynman, R.P., Leighton, R.B., Sands, M. (Eds.), Feynman Lectures on Physics. Addison-Wesley, Reading, MA.

Hunten, D.M., Roach, F.E., Chamberlain, J.W., 1956. A photometric unit for the airglow and aurora. Journal of Atmospheric and Terrestrial Physics 8, 345–346.

Hunten, D.M., Shemansky, D.E., Morgan, T.H., 1988. The Mercury atmosphere, in: Vilas F., Chapman C.R., Matthews M.S. (Eds.), Mercury, University of Arizona Press. pp. 562–612.

Ip, W.H., 1986. The sodium exosphere and magnetosphere of Mercury. Geophys. Res. Lett. 13, 423–426. doi:10.1029/GL013i005p00423

Johnson, R.E., 1990. Energetic Charged-Particle Interactions with Atmospheres and Surfaces. Springer-Verlag, New York.

Johnson, R.E., Leblanc, F., Yakshinskiy, B.V., Madey, T.E., 2002. Energy Distributions for Desorption of Sodium and Potassium from Ice: The Na/K Ratio at Europa. Icarus 156, 136–142. doi:10.1006/icar.2001.6763

Kameda, S., Yoshikawa, I., Kagitani, M., Okano, S., 2009. Interplanetary dust distribution and temporal variability of Mercury's atmospheric Na.

Geophys. Res. Lett. 36, L15201. doi:10.1029/2009GL039036

Killen, R., Cremonese, G., Lammer, H., Orsini, S., Potter, A.E., Sprague, A.L., Wurz, P., Khodachenko, M.L., Lichtenegger, H.I.M., Milillo, A., Mura, A., 2007. Processes that Promote and Deplete the Exosphere of Mercury. Space Sci. Rev. 132, 433–509. doi:10.1007/s11214-007-9232-0

Killen, R.M., 2006. Curve-of-Growth Model for Sodium D_2 Emission at Mercury. Publications of the Astronomical Society of the Pacific 118, 1344–1350. doi:10.1086/508070

Killen, R.M., Mouawad, N., Shemansky, D.E., 2009. Expected Emission from Mercury's Exospheric Species, and their Ultraviolet-Visible Signatures. The Astrophysical Journal Supplement Series 181, 351.

Killen, R.M., Potter, A., Fitzsimmons, A., Morgan, T.H., 1999. Sodium D_2 line profiles: clues to the temperature structure of Mercury's exosphere. Planet. Space Sci. 47, 1449–1458. doi:10.1016/S0032-0633(99)00071-9

Killen, R.M., Potter, A.E., Reiff, P., Sarantos, M., Jackson, B.V., Hick, P., Giles, B., 2001. Evidence for space weather at Mercury. J. Geophys. Res. 106, 20509–20525. doi:10.1029/2000JE001401

Killen, R.M., Sarantos, M., Potter, A.E., Reiff, P., 2004. Source rates and ion recycling rates for Na and K in Mercury's atmosphere. Icarus 171, 1–19. doi:10.1016/j.icarus.2004.04.007

Lammer, H., Wurz, P., Patel, M.R., Killen, R., Kolb, C., Massetti, S., Orsini, S., Milillo, A., 2003. The variability of Mercury's exosphere by particle and radiation induced surface release processes. Icarus 166, 238–247.

doi:10.1016/j.icarus.2003.08.012

Leblanc, F., Chaufray, J.Y., Doressoundiram, A., Berthelier, J.J., Mangano, V., Lopez-Ariste, A., Borin, P., 2013. Mercury exosphere. III: Energetic characterization of its sodium component. Icarus 223, 963–974. doi:10.1016/j.icarus.2012.08.025

Leblanc, F., Doressoundiram, A., Schneider, N.M., Massetti, S., Wedlund, M., Lopez Ariste, A., Barbieri, C., Mangano, V., Cremonese, G., 2009. Short-term variations of Mercury's Na exosphere observed with very high spectral resolution. Geophys. Res. Lett. 36, L07201. doi:10.1029/2009GL038089

Leblanc, F., Johnson, R.E., 2003. Mercury's sodium exosphere. Icarus 164, 261–281. doi:10.1016/S0019-1035(03)00147-7

Leblanc, F., Johnson, R.E., 2010. Mercury exosphere I. Global circulation model of its sodium component. Icarus 209, 280–300. doi:10.1016/j.icarus.2010.04.020

Mangano, V., Leblanc, F., Barbieri, C., Massetti, S., Milillo, A., Cremonese, G., Grava, C., 2009. Detection of a southern peak in Mercury's sodium exosphere with the TNG in 2005. Icarus 201, 424–431. doi:10.1016/j.icarus.2009.01.016

Mangano, V., Massetti, S., Milillo, A., Mura, A., Orsini, S., Leblanc, F., 2013. Dynamical evolution of sodium anisotropies in the exosphere of Mercury. Planetary and Space Science 82–83, 1–10. doi:10.1016/j.pss.2013.03.002

Markwardt, C.B., 2009. Non-Linear Least Squares Fitting in IDL with MPFIT, in: Bohlender, D., Dowler, P., Durand, D. (Eds.), pp. 251–254.

McClintock, W.E., Lankton, M.R., 2007. The Mercury Atmospheric and Surface Composition Spectrometer for the MESSENGER Mission. Space Science Reviews 131, 481–521. doi:10.1007/s11214-007-9264-5

McGrath, M.A., Johnson, R.E., Lanzerotti, L.J., 1986. Sputtering of sodium on the planet Mercury. Nature 323, 694–696. doi:10.1038/323694a0

Mouawad, N., Burger, M.H., Killen, R.M., Potter, A.E., McClintock, W.E., Vervack Jr., R.J., Bradley, E.T., Benna, M., Naidu, S., 2011. Constraints on Mercury's Na exosphere: Combined MESSENGER and ground-based data. Icarus 211, 21–36. doi:10.1016/j.icarus.2010.10.019

Mura, A., Wurz, P., Lichtenegger, H.I.M., Schleicher, H., Lammer, H., Delcourt, D., Milillo, A., Orsini, S., Massetti, S., Khodachenko, M.L., 2009. The sodium exosphere of Mercury: Comparison between observations during Mercury's transit and model results. Icarus 200, 1–11. doi:10.1016/j.icarus.2008.11.014

Oura, K., Lifshits, V., Saranin, A., Zotov, A., Katayama, M., 2003. Surface Science: An Introduction (Advanced Texts in Physics). Springer.

Potter, A.E., Killen, R.M., Morgan, T.H., 2007. Solar radiation acceleration effects on Mercury sodium emission. Icarus 186, 571–580. doi:10.1016/j.icarus.2006.09.025

Potter, A.E., Killen, R.M., Reardon, K.P., Bida, T.A., 2013. Observation of neutral sodium above Mercury during the transit of November 8, 2006. Icarus 226, 172–185. doi:10.1016/j.icarus.2013.05.029

Potter, A.E., Killen, R.M., Sarantos, M., 2006. Spatial distribution of sodium on

Mercury. Icarus 181, 1–12. doi:10.1016/j.icarus.2005.10.026

Potter, A.E., Morgan, T.H., 1985. Discovery of Sodium in the Atmosphere of Mercury. Science 229, 651–653. doi:10.1126/science.229.4714.651

Potter, A.E., Morgan, T.H., 1987. Variation of sodium on mercury with solar radiation pressure. Icarus 71, 472–477. doi:10.1016/0019-1035(87)90041-8

Potter, A.E., Morgan, T.H., 1990. Evidence for Magnetospheric Effects on the Sodium Atmosphere of Mercury. Science 248, 835–838. doi:10.1126/science.248.4957.835

Sarantos, M., Killen, R.M., Kim, D., 2007. Predicting the long-term solar wind ion-sputtering source at Mercury. Planet. Space Sci. 55, 1584–1595. doi:10.1016/j.pss.2006.10.011

Sarantos, M., Killen, R.M., Sharma, A.S., Slavin, J.A., 2008. Influence of plasma ions on source rates for the lunar exosphere during passage through the Earth's magnetosphere. Geophys. Res. Lett. 35, L04105. doi:10.1029/2007GL032310

Sarantos, M., Killen, R.M., Surjalal Sharma, A., Slavin, J.A., 2010. Sources of sodium in the lunar exosphere: Modeling using ground-based observations of sodium emission and spacecraft data of the plasma. Icarus 205, 364–374. doi:10.1016/j.icarus.2009.07.039

Sarantos, M., Reiff, P.H., Hill, T.W., Killen, R.M., Urquhart, A.L., 2001. A Bx-interconnected magnetosphere model for Mercury. Planet. Space Sci. 49, 1629–1635. doi:10.1016/S0032-0633(01)00100-3

Schleicher, H., Wiedemann, G., Wohl, H., Berkefeld, T., Soltau, D., 2004. Detection of neutral sodium above Mercury during the transit on 2003 May 7. Astron. Astrophys. 425, 1119–1124. doi:10.1051/0004-6361:20040477

Schmidt, C.A., 2013. Monte Carlo modeling of north-south asymmetries in Mercury's sodium exosphere. J. Geophys. Res. Space Physics 118, 4564–4571. doi:10.1002/jgra.50396

Schmidt, C.A., Baumgardner, J., Mendillo, M., Wilson, J.K., 2012. Escape rates and variability constraints for high-energy sodium sources at Mercury. J. Geophys. Res. 117, A03301. doi:10.1029/2011JA017217

Smyth, W.H., 1986. Nature and variability of Mercury's sodium atmosphere. Nature 323, 696–699. doi:10.1038/323696a0

Smyth, W.H., Marconi, M.L., 1995. Theoretical overview and modeling of the sodium and potassium atmospheres of mercury. Astrophys.J. 441, 839–864. doi:10.1086/175407

Sprague, A.L., Kozlowski, R.W.H., Hunten, D.M., Schneider, N.M., Domingue, D.L., Wells, W.K., Schmitt, W., Fink, U., 1997. Distribution and Abundance of Sodium in Mercury's Atmosphere, 1985-1988. Icarus 129, 506–527. doi:10.1006/icar.1997.5784

Sprague, A.L., Schmitt, W.J., Hill, R.E., 1998. Mercury: Sodium Atmospheric Enhancements, Radar-Bright Spots, and Visible Surface Features. Icarus 136, 60–68. doi:10.1006/icar.1998.6009

Vervack, R.J., McClintock, W.E., Killen, R.M., Sprague, A.L., Anderson, B.J., Burger, M.H., Bradley, E.T., Mouawad, N., Solomon, S.C., Izenberg, N.R., 2010.

Mercury's Complex Exosphere: Results from MESSENGER's Third Flyby. Science 329, 672–675. doi:10.1126/science.1188572

Wang, Y.C., Ip, W.H., 2011. Source dependency of exospheric sodium on Mercury. Icarus 216, 387–402. doi:10.1016/j.icarus.2011.09.023

Winslow, R.M., Johnson, C.L., Anderson, B.J., Korth, H., Slavin, J.A., Purucker, M.E., Solomon, S.C., 2012. Observations of Mercury's northern cusp region with MESSENGER's Magnetometer. Geophys. Res. Lett. 39, L08112. doi:10.1029/2012GL051472

Wurz, P., Whitby, J.A., Rohner, U., Martin-Fernandez, J.A., Lammer, H., Kolb, C., 2010. Self-consistent modelling of Mercury's exosphere by sputtering, micro-meteorite impact and photon-stimulated desorption. Planet. Space Sci. 58, 1599–1616. doi:10.1016/j.pss.2010.08.003

Yakshinskiy, B.V., Madey, T.E., 1999. Photon-stimulated desorption as a substantial source of sodium in the lunar atmosphere. Nature 400, 642–644. doi:10.1038/23204

Yakshinskiy, B.V., Madey, T.E., 2004. Photon-stimulated desorption of Na from a lunar sample: temperature-dependent effects. Icarus 168, 53–59. doi:10.1016/j.icarus.2003.12.007

Yakshinskiy, B.V., Madey, T.E., 2005. Temperature-dependent DIET of alkalis from SiO_2 films: Comparison with a lunar sample. Surf. Sci. 593, 202–209. doi:10.1016/j.susc.2005.06.062

Yakshinskiy, B.V., Madey, T.E., Ageev, V.N., 2000. Thermal Desorption of Sodium Atoms from Thin SiO_2 Films. Surf. Rev. Lett. 07, 75–87.

doi:10.1142/S0218625X00000117

Yan, N., Chassefire, E., Leblanc, F., Sarkissian, A., 2006. Thermal model of Mercury's surface and subsurface: Impact of subsurface physical heterogeneities on the surface temperature. Adv. Space Res. 38, 583–588. doi:10.1016/j.asr.2005.11.010

Zuber, M.T., Aharonson, O., Aurnou, J.M., Cheng, A.F., Ii, S.A.H., Heimpel, M.H., Neumann, G.A., Peale, S.J., Phillips, R.J., Smith, D.E., Solomon, S.C., Stanley, S., 2007. The Geophysics of Mercury: Current Status and Anticipated Insights from the MESSENGER Mission. Space Sci. Rev. 131, 105–132. doi:10.1007/s11214-007-9265-4

Appendix 1: Verification of the model fits

In this appendix we describe tests of the assumptions described in the main text. The first of these is our assumption that the g-value for exospheric sodium is close to the g-value at Mercury's rest frame (Eq. 1). We also test the expressions used to estimate exospheric temperature and density (Eqs. 2-4). We used the Monte Carlo model developed by Burger et al. (2010, 2012, 2014) for these tests. We ejected sodium from the surface with a Maxwell-Boltzmann flux distribution at several different temperatures and for several different true anomalies to obtain a range of g-values. The loss processes in the model are photoionization and sticking; atoms are removed from the simulation if their trajectories intersect Mercury's surface. We also ran cases with thermal accommodation in place of sticking. We used accommodation coefficients of 0.2 and 0.9.

To test the constant g-value assumption we compared the model's calculated column density N and radiance $4\pi I$ to test the accuracy of Eq. (1) when using the g-value in Mercury's rest frame. If this approximation is valid then the ratio $Ng/4\pi I$ should be close to 1. For a model run with globally uniform sodium emission at 1200 K, that ratio is within a few percent of 1 near noon, and within 10% of 1 near the terminator. Even at 5000 K the results are similar (when excluding the escaping component at high altitudes). We also considered the case of non-uniform exosphere in which we used a source rate proportional to

the cosine of the solar zenith angle. We found that the ratio is again close to 1 near noon, but that it differs from unity by up to 25% near the terminator for the cases with the largest *g*-values.

The ratio was also close to 1 for cases with thermal accommodation. This might not be the case with other models if they assume that partially-accommodated atoms retain their transverse momentum. In that case the atoms can build up more speed as they are transported anti-sunward. Our model assumes that atoms are scattered in a random direction after accommodation. Under those circumstances the simulated sodium atoms do not pick up speed as they are accelerated anti-sunward except in the extreme case of an accommodation coefficient of 0, as demonstrated by Mouawad et al. (2011).

To test the temperature estimate (fits to Eqs. 2-4) we simulated limb scans with the Monte Carlo model. The model replicates the actual observation geometry used by UVVS, allowing us to "fly" the instrument through exosphere simulations. An example comparison between the Monte Carlo model and Eq. (2) is shown in Fig. 12. The agreement between the slopes of the two curves is quite good, suggesting that Eq. (2) captures the physics of the sodium exosphere quite accurately despite the approximations made in using Eqs. (1)–(4), such as the assumption that the *g*-value and photon acceleration *b* are independent of sodium atom speed. We also ran these simulated limb scans through the fitting routine described in the paper and returned the correct temperature to within 100 K.

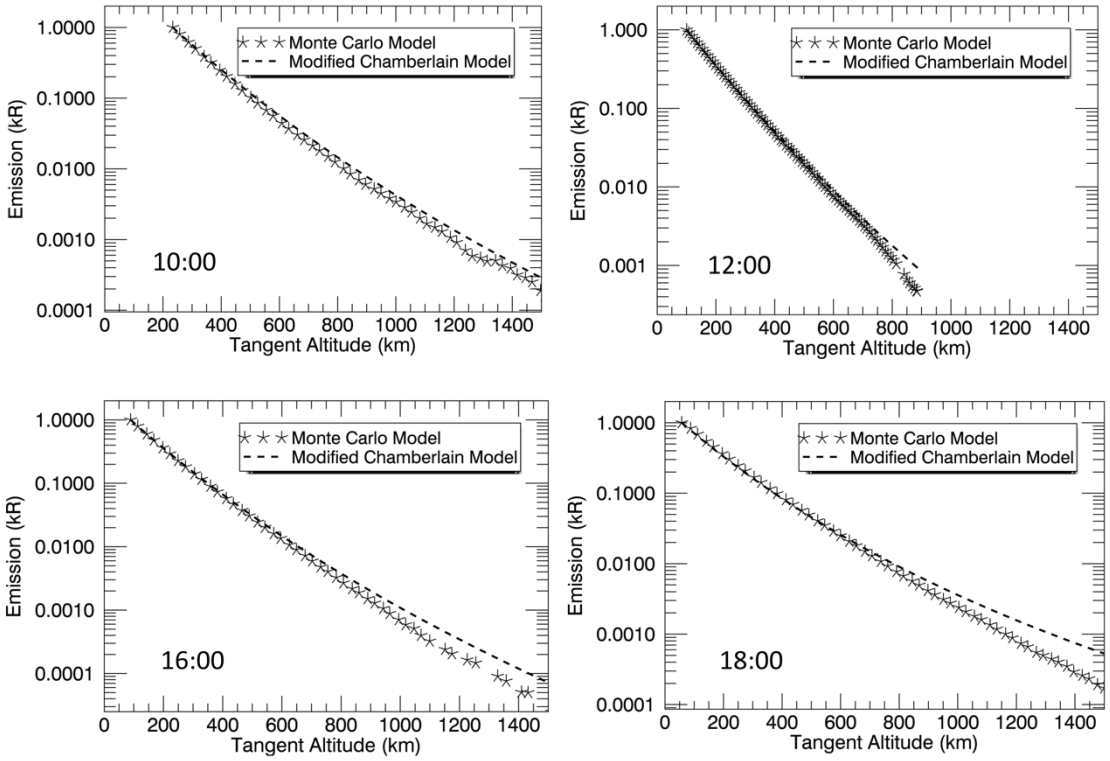

Fig. 12. Comparison of Monte Carlo model (data points) with the model given by Eqs. (2)-(4) (dashed line). The Monte Carlo model, in this example, used the observational geometry from limb scans taken on 6 August 2012.

Appendix 2: Optical depth correction

Here we describe a simple analytic correction for optical depth near the surface. Optical depth causes some of the emitted photons to be scattered before reaching the detector, which lowers the apparent column density. The correction was applied to the data before fitting to Eq. (2). It has almost no effect on most of the data, which are usually acquired along a optically thin lines of

sight. Fig. 13 shows that the correction applied to Eq. (2) matches the slight turnover in apparent column density near the surface. The correction only works only for modest line-of-sight optical depths (on the order of 1); larger optical depths require detailed calculations (Killen, 2006; Chaufray and Leblanc, 2013). The correction clearly breaks down (does not match data) for the largest columns in Fig. 13.

The correction is derived from a few simple assumptions. The first of these is that each sodium atom is emitting photons at the rate of g s^{-1}. This assumption is true only if the exosphere is illuminated by unattenuated sunlight, which is appropriate if we apply the correction only in situations with low optical depths. UVVS limb scans look tangent to the surface, resulting in line-of-sight column densities much larger than those traversed by sunlight. A line-of-sight column is only about one-tenth of the vertical column (factor $2K$ in Eq. 2). This factor means that sunlight traverses one-tenth of the line-of-sight column at noon local time, whereas at mid-morning and mid-afternoon that value is about 50% larger; this larger figure is still much less than for the line-of-sight column. Even at the terminator, where incident sunlight is tangent to the surface, the column traversed by sunlight is only half of the line-of-sight column. Because we apply this correction for line-of-sight optical depths on the order of unity or less, we ensure that sunlight traverses negligible optical depths. We also assume that the photons are emitted isotropically, though the D_2 emission is slightly anisotropic (Chamberlain, 1961).

Suppose we are looking at emission from a column of uniformly illuminated

atoms with optical depth τ along the line of sight. The fraction of photons F that make it out of the column without being scattered is given by

$$F = \frac{1}{\tau}\int_0^{\tau} \mathrm{e}^{-\tau}\,\mathrm{d}\tau$$

where the integrand is the probability that a photon will not be scattered while passing through an optical depth τ. The factor in front is a normalization constant. The optical depth τ is directly proportional to the column density N, with the constant of proportionality coming from Brown and Yung (1976). That constant is a weak function of temperature, for which we used 1200 K except for the simulated thermal components, for which we used the temperatures indicated in Fig. 8. The sodium D_1 and D_2 lines are distinct lines so F must be calculated separately for each line.

The intensity (units of cm^{-2} s^{-1} sr^{-1}) of photons that are not scattered is given by $(Ng/4\pi)F$, where the symbols are defined in the main text. This expression suggests that the radiance, which is given by 4π times the intensity, is attenuated by the factor F, but scattered photons also contribute to the intensity. To calculate the intensity of scattered photons we assume they are scattered only once, as appropriate for small optical depths. We also assume that the photons come from a plane-parallel column of gas. Given these assumptions the intensity of scattered photons is given by $(Ng/4\pi)(1-F)/4$, which we calculate as follows. The flux of photons produced by the plane of gas in the absence of scattering is given by the intensity multiplied by π: $(Ng/4\pi)\pi$. A fraction (1-F) of these are scattered approximately uniformly into 4π radians (Killen et al., 2009). The resulting intensity of scattered photons is found by dividing the flux by 4π

radians to yield $(Ng/4\pi)\pi(1-F)/4\pi$.

Putting this all together, the total intensity from both scattered and unscattered photons is given by $(Ng/4\pi)(F+(1-F)/4)$, which means that the intensity $(Ng/4\pi)$ of photons produced in the exosphere is reduced by the factor $(F+(1-F)/4)$, with F, the fraction of photons that are scattered. Fig. 13 shows the correction applied to limb scan fits. One example is from near perihelion, when some of the largest optical depths were observed, and the other is more typical with much lower optical depths. We multiplied the model column density (dashed black line) by the factor $(F+(1-F)/4)$. The corrected column density (blue line) matches the data for moderate optical depths ($\tau \leq 2$ for the D_1 line).

The correction starts to break down when the optical depth is large, i.e., when the assumptions of single scattering and unattenuated sunlight break down. Note that an optical depth of 1 corresponds to a column density (black dashed line) of $\sim 2\times10^{11}$ cm^{-2} for the D_1 line or $\sim 4\times10^{11}$ cm^{-2} for the D_2 line.

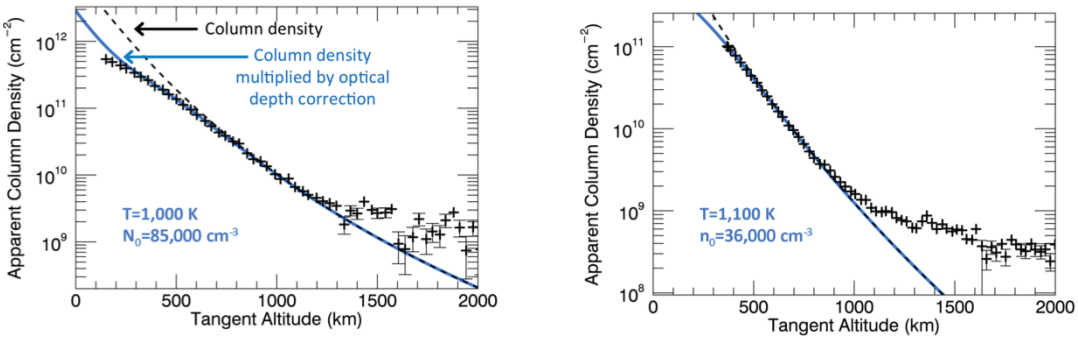

Fig. 13. Examples of the optical depth correction. Limb scan fits with and without the optical depth correction applied, as indicated. The apparent column density (blue line) is lower than the actual column density (black dashed line). The fit parameters are given in the lower left of each panel. Note that the optical depth correction breaks down near the surface in the left panel,

where the data points and blue line diverge.

The optical depth correction was applied to the data before fitting with Eq. (2). We used only those data for which the D_1 emission line optical depth is less than 1 in the fitting routine. The effect of this correction on our analysis is minimal for most of the data, but it is necessary to probe the moderate optical depths where colder gas may reside. The consistent agreement between the data and model at moderate optical depths suggests that the optical depth correction is reasonably accurate and useful, but it is still a simple approximation of the actual photon transport problem. For that reason, we do not rule out the presence of a low-altitude, low-temperature component of the exosphere.